



Adsorption/photocatalytic activity and fundamental natures of BiOCl and BiOCl_xI_{1-x} prepared in water and ethylene glycol environments, and Ag and Au-doping effects

Won Joo Kim^a, Debabrata Pradhan^b, Bong-Ki Min^c, Youngku Sohn^{a,*}

^a Department of Chemistry, Yeungnam University, Gyeongsan 712-749, Republic of Korea

^b Materials Science Centre, Indian Institute of Technology, Kharagpur 721 302, W.B., India

^c Instrumental Analysis Center, Yeungnam University, Gyeongsan 712-749, Republic of Korea



ARTICLE INFO

Article history:

Received 26 June 2013

Received in revised form 3 October 2013

Accepted 7 October 2013

Available online 15 October 2013

Keywords:

BiOCl

BiOCl_xI_{1-x}

Doping

Adsorption

Photocatalytic degradation

ABSTRACT

BiOCl and BiOCl_xI_{1-x} were synthesized in two different solvents of ethylene glycol (EG) and water, and their natures were examined by scanning electron microscopy (SEM), electron transmission microscopy (TEM), X-ray diffraction, UV-vis absorption and Raman, Fourier-transform infrared, and photoluminescence spectroscopy. The Ag and Au-doping effects on the fundamental nature and photocatalytic activity of BiOCl and BiOCl_xI_{1-x} were investigated in detail. SEM revealed that 3D flower-like and 2D plate-like microstructures were formed with EG and water solvents, respectively. The as-synthesized samples were tested for the adsorption and photocatalytic degradation of methyl orange and Rhodamine B, with the flower-like 3D-structure showing superior adsorption performance relative to the stacked 2D plate-like structures. Upon introducing iodine into BiOCl, we observed a dramatic increase in the adsorption ability and Brunauer–Emmett–Teller surface area, with an order of 2D BiOCl < 3D BiOCl ≪ BiOCl_xI_{1-x} ($x = 0.8, 0.6$ and 0.4). The dye degradation performance was further markedly enhanced under irradiation by visible light. However, a small amount of Ag and Au-doping drastically negated the adsorption and photocatalytic performance. The photocatalytic mechanism was elucidated by an indirect chemical probe method using active species scavengers, and photoluminescence spectroscopy. On the basis of the results obtained, we propose a dye-sensitized photodegradation mechanism, and the active species play roles in the order of •OH ≪ •O₂⁻ ≈ h⁺ under visible light irradiation.

© 2013 Elsevier B.V. All rights reserved.

1. Introduction

Removing hazardous materials (or pollutants) from water has become increasingly important to obtain drinkable water (or usable pure solvent) resources. In recent years, bismuth oxyhalides BiOX (X = Cl, Br, I) have been extensively studied and demonstrated as outstanding adsorption/photocatalytic dye removal materials [1–20]. It is commonly believed that the catalytic performance and adsorption ability are highly dependent on the exposed crystal facets, morphology and size of catalysts. Wet chemical (more conveniently) and dry physical methods are commonly employed to synthesize various shapes of BiOCl such as plates, flowers, flakes [12,20], hollow microspheres [12], nanowires and films [1,22]. The electrochemical deposition method was recently utilized to obtain a thin BiOCl film with highly {1 1 0} exposed facets by Zhang et al. [1]. Additionally, Li et al. prepared BiOCl film on a Ti substrate by reacting Bi₂O₃ film with Cl⁻ under acidic

conditions [3]. Tian et al. prepared BiOCl nanowires from β-Bi₂O₃ via liquid phase growth involving $\text{Bi}_2\text{O}_3 + 6\text{HCl} \rightarrow 2\text{BiCl}_3 + 3\text{H}_2\text{O}$ and $2\text{BiCl}_3 + 2\text{H}_2\text{O} \rightarrow 2\text{BiOCl} + 4\text{HCl}$ chemical reactions [16]. Among bismuth oxyhalides, BiOCl has been used as a catalyst for the decomposition of various dyes such as methyl orange (MO) and Rhodamine B (RhB), toxic pollutants such as phenols and potassium dichromate, and oxidative cracking of alkanes. It is important to note that, under visible light irradiation, BiOCl was shown to have a higher photodegradation performance than TiO₂ [13]. The catalytic activity can be further increased for hybridized BiOCl such as Cu(II) phthalocyanine (CuPc) combined with BiOCl [2]. The increase in visible light photocatalytic activity (dye degradation and hydrogen evolution) has been attributed to an excited electron transfer process from CuPc to BiOCl [2]. Photocatalytic MO degradation performance of BiOCl was further improved by introducing Bi into the catalyst, where it may enhance light absorption, charge separation efficiency, and the charge transfer rate [5]. Gao et al. showed that the photodegradation of methylbenzene can be enhanced by loading graphene due to enhanced charge separation efficiency by C-Bi chemical coupling [11]. Heterojunction BiOCl/Bi₂O₃ has also been shown to exhibit dramatic photocatalytic efficiency for

* Corresponding author. Tel.: +82 53 810 2354; fax: +82 53 810 4613.

E-mail address: youngkusohn@ynu.ac.kr (Y. Sohn).

decomposing organic compounds. The electrons in the conduction band (CB) of BiOCl transfer to Bi₂O₃, consequently the holes in the valence band (VB) initiate oxidation reactions [24]. The photocatalytic activity for different dyes has also been shown to be determined by the relative composition of BiOCl/BiOI. For example, 20% and 70% BiOCl/BiOI composites showed the highest catalytic performance for the decomposition of MO and RhB, respectively [17].

The bandgap and type of vacancies (defects) are known to play important roles in the photocatalytic behavior of catalyst materials. The band gap of BiOCl was reported to decrease upon loading Bi₂S₃ by a controlled anion exchange approach. In this system, Bi₂S₃ absorbs visible light because of a lower bandgap, after which its energy transfers to the conduction band of BiOCl, and consequently further enhances the visible light photocatalytic decomposition efficiency of 2,4-dichlorophenol in water [8]. During the photocatalytic reaction, oxygen vacancy was shown to play a significant role in the photocatalytic efficiency. Ye et al. obtained black (from white color) BiOCl by creating oxygen vacancies under UV irradiation and observed 20 times higher activity for the visible light photodegradation of RhB [9].

In the present study, in addition to the synthesis and photocatalytic activity of BiOCl, we synthesized BiOCl_xI_{1-x} ($x=0.8, 0.6$ and 0.4) structures in two different solvents, water and ethylene glycol (EG), and examined their fundamental natures and adsorption/photocatalytic performances in detail. Furthermore, we doped the BiOCl and BiOCl_xI_{1-x} nanostructures with Ag and Au to examine the doping effects on the fundamental natures and adsorption/photocatalytic activity of BiOCl and BiOCl_{0.6}I_{0.4} compounds. The photodegradation mechanism in presence different as-synthesized BiOCl catalysts under UV and visible lights is proposed on the basis of the results obtained with/without active species scavengers and photoluminescence spectroscopy.

2. Experimental

2.1. Catalysts preparation

BiOCl_xI_{1-x} ($x=1, 0.8, 0.6$, and 0.4) were synthesized as follows. We first completely dissolved stoichiometric amounts of Bi(NO₃)₃, KCl, and KI in 25 mL Millipore water of 18.2 MΩ-cm resistivity (or in 25 mL EG), after which we transferred them to a 120 mL Teflon-lined stainless steel autoclave. The autoclave was then placed in an oven (120 °C) for 12 h. The final products were subsequently centrifuged, washed with Millipore water and ethanol several times, and dried in an oven (80 °C) for further characterization.

2.2. Catalysts characterization

The surface morphology of the samples was examined by scanning electron microscopy (SEM, Hitachi SE-4800). The powder X-ray diffraction (XRD) patterns were obtained using a PANalytical X'Pert Pro MPD diffractometer with Cu Kα radiation (40 kV and 30 mA). For the transmission electron microscopic (TEM) and high resolution TEM (HRTEM) study, the catalyst was placed on a carbon-coated Cu grid. The TEM/HRTEM images and electron diffraction patterns were taken using a FEI Tecnai G2 F20 TEM operated at 200.0 kV. Energy-dispersive X-ray spectroscopy (EDX) data were obtained to analyze elemental composition. The UV-vis absorption characteristics (or band gaps) were examined using a Varian Cary 5000 UV-vis-near IR (UV-vis-NIR) spectrophotometer for powder samples. The Raman spectra for pelletized samples were taken using a Bruker Senterra Raman spectrometer with a laser excitation energy of 532 nm. The Fourier-transform infrared (FT-IR) measurements were carried out using a Thermo Scientific Nicolet iS10

spectrometer. The photoluminescence spectra were collected using a SCINCO FluoroMate FS-2. The Brunauer–Emmett–Teller (BET) surface area measurements were performed using a Quantachrome ChemBET TPR/TPD analyzer equipped with a thermal conductivity detector.

2.3. Adsorption, photocatalytic activity and mechanism analysis

For the adsorption and photocatalytic reactions, we dispersed 50 mg of a catalyst into a 100 mL dye (MO and RhB) solution with dye concentrations of 10, 20 and 50 mg/L. We stirred the dye solution during an adsorption test in the dark and during the photocatalytic experiments in the presence of different types of light. For the photocatalytic experiments, we used a light (mixed fluorescent light and sunlight passing through a window of our laboratory) and incandescent light to simulate a daylight dye degradation process. The UV-vis absorption intensity of the dye solution was measured with a Jasco V-530 UV-vis spectrophotometer. To detect the roles of active species (•OH, •O₂⁻ and h⁺), isopropyl alcohol (IPA), benzoquinone (BQ) and EDTA were added in the dye solution, as scavengers for •OH, •O₂⁻ and h⁺, respectively [25–27]. After irradiation of UV ($\lambda < 420$ nm) or visible ($\lambda > 420$ nm) light, we measured the UV-vis absorption intensity of the dye solution. To detect active •OH radicals, we dispersed the catalyst in a terephthalic acid solution [26], and irradiated UV or visible light. After the photoirradiation, the photoluminescence of the corresponding dye solution was measured at an excitation wavelength of 315 nm using a SCINCO FluoroMate FS-2.

3. Results and discussion

3.1. Morphology

The left and right column of Fig. 1 show the SEM images of BiOCl_xI_{1-x} ($x=1, 0.8, 0.6$, and 0.4) prepared in EG and water solvents, respectively. In the inset of the SEM images, the optical images of the respective samples are displayed. The middle column of Fig. 1 shows the magnified SEM images shown in the left column. As shown in the SEM images, the morphologies of BiOCl samples were found to differ drastically by varying the reaction medium (i.e. solvents). The BiOCl prepared in EG showed 3D flower-like globular hierarchical structures of 1–3 μm in size, while that in water showed stacked 2D plate-like structures <100 nm thick. For the iodine-containing BiOCl_xI_{1-x} samples prepared in EG, the morphology was found to be very similar to that of BiOCl prepared in EG. However, the color of samples became dark yellow with increasing iodine composition, as shown in the inset optical images. For the BiOCl_xI_{1-x} samples prepared in water, the morphology changed to individual 2D wall-like structures with increasing iodine composition. The change in color was not drastic with increasing iodine, and the color of BiOCl_{0.4}I_{0.6} was pale yellow. The morphology of BiOCl prepared in ethanol was similar to that of BiOCl obtained in water (Supporting Info. Fig. S1).

3.2. Crystal structure and microstructure

Fig. 2 displays the powder XRD patterns of BiOCl_xI_{1-x} ($x=1, 0.8, 0.6$, and 0.4) samples prepared in EG and water medium. The XRD patterns of samples prepared in EG matched those of tetragonal (P4/nmm) BiOCl (JCPDS 6-0249) well. The XRD peaks of samples prepared in water were 11.5 times sharper and stronger for the (001) plane and 2.37 times sharper and stronger for the (011) plane, and matched those of tetragonal (P4/nmm) BiOCl (JCPDS 1-073-2060) well. A major difference between the BiOCl samples is that the (001) peak was dominant for the 2D plate-like structure (synthesized in water), while the (011) and (110) peaks prevailed for

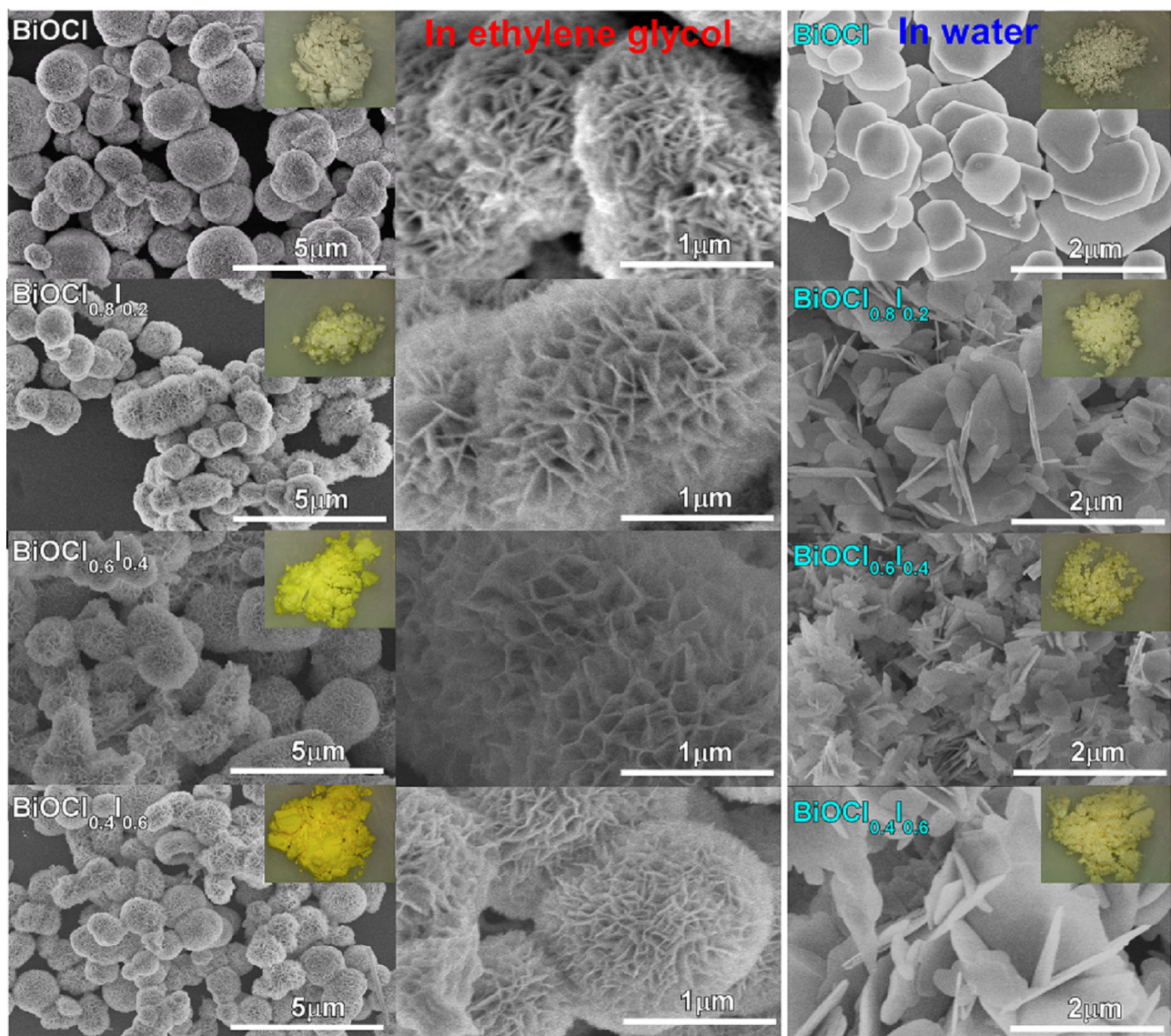


Fig. 1. SEM images of $\text{BiOCl}_x\text{I}_{1-x}$ ($x = 1, 0.8, 0.6$, and 0.4) prepared in EG (left two columns) and water (right column). Inset optical microscopy images show the color of the corresponding samples. (For interpretation of the references to color in this figure legend, the reader is referred to the web version of the article.)

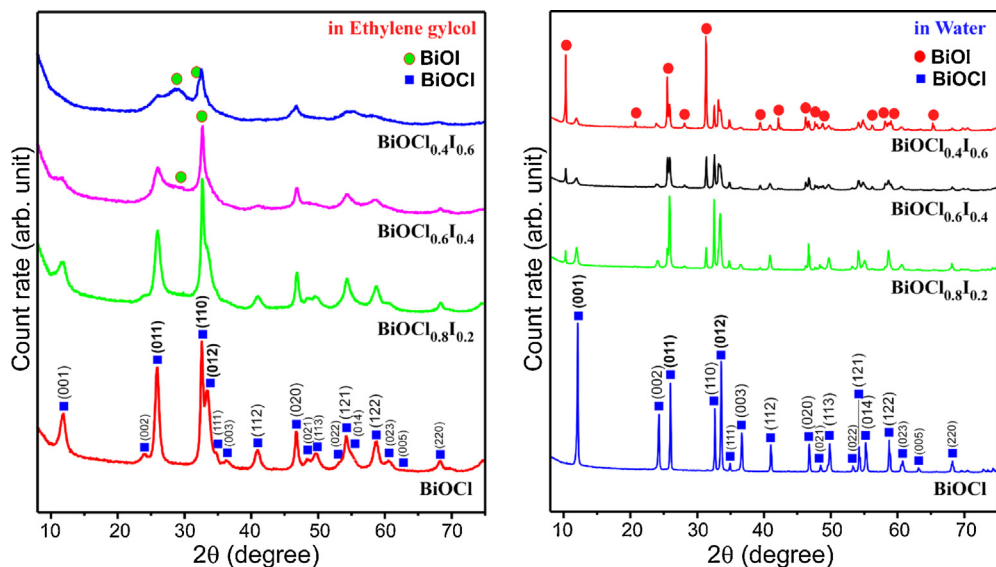


Fig. 2. Power X-ray diffraction patterns of $\text{BiOCl}_x\text{I}_{1-x}$ ($x = 1, 0.8, 0.6$, and 0.4) prepared in EG and water.

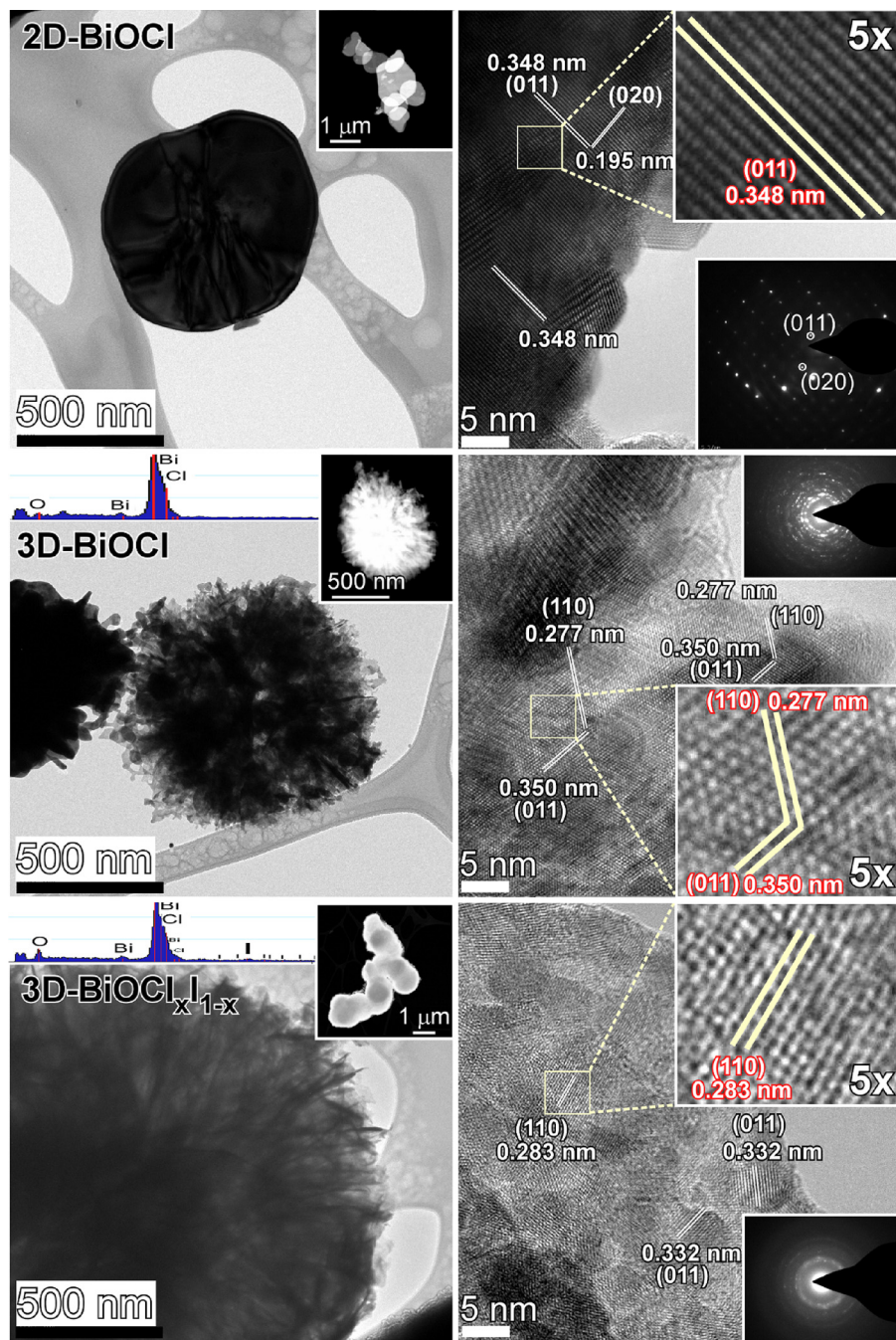


Fig. 3. TEM (left column), HRTEM (right column) and high-angle annular dark field (HAADF) TEM image (inset, left column) of 2D-BiOCl, 3D-BiOCl and 3D-BiOCl_{0.6}I_{0.4} samples. EDX results (inset, left column) show the elemental composition of 3D-BiOCl and 3D-BiOCl_{0.6}I_{0.4} samples. Insets (right column) show the corresponding electron diffraction patterns.

the 3D flower-like structure (synthesized in EG). The (001)/(011) ratios for the 3D flower-like and 2D plate-like BiOCl were 0.34 and 1.67, respectively. These findings indicate that the 2D plate-like structures had fewer {001} exposed facets. For the 2D plate-like BiOCl prepared in ethanol, the (001)/(011) ratio was dramatically increased to 4.1 (Supporting Info. Fig. S2). Three major peaks were found at $2\theta = 12.03^\circ$, 24.16° and 36.57° , corresponding to the (001), (002) and (003) planes, respectively. Upon introduction of iodine for the 3D flower-like structures, the XRD features became much broader, indicating decreased crystallinity. This is believed to be due to the formation of an amorphous/semicrystalline phase in EG solvent that shows broader diffraction for BiOI in BiOCl_{0.4}I_{0.6}. For the 2D plate-like structures, the XRD patterns clearly show

very sharp and distinct diffraction of the BiOI phase with increasing iodine composition. These findings indicate the formation of a highly crystalline BiOI phase in BiOCl_xI_{1-x} in the water medium.

The TEM and HRTEM images of three selected samples (2D-BiOCl, 3D-BiOCl and 3D-BiOCl_{0.6}I_{0.4}) are displayed in Fig. 3. The HRTEM image of 2D-BiOCl clearly showed two lattice fringes with spacings of 0.348 nm and 0.195 nm, corresponding to {011} and {020} facets, respectively. The selected area electron diffraction (SAED) pattern clearly reflects a highly single crystalline nature of the catalyst, and the {011} and {020} facets. These results reflect higher percentage of {001} facets, as discussed in the XRD results in Fig. 2. For the 3D-BiOCl (EG) and 3D-BiOCl_{0.6}I_{0.4} (EG) catalysts, the TEM images showed a flower-like structure. The less crystalline

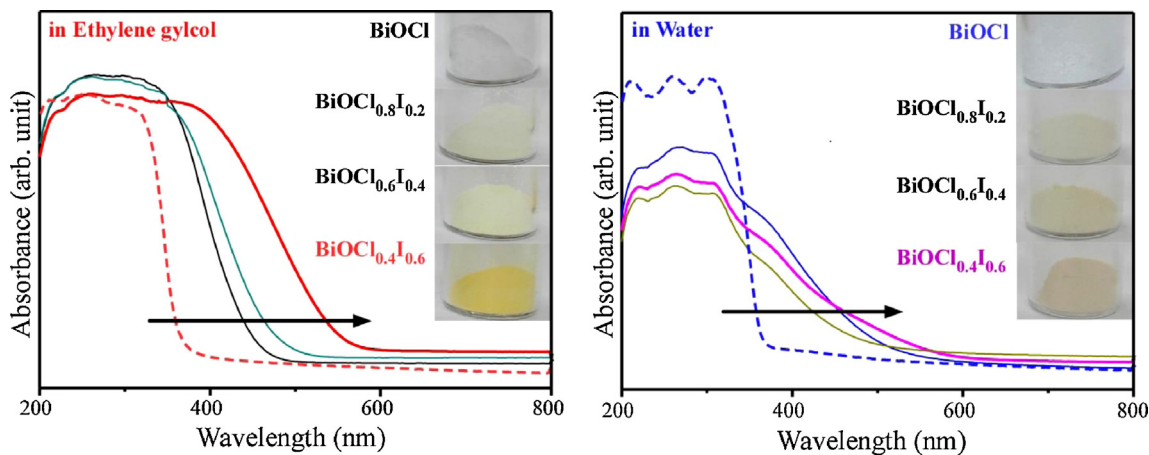


Fig. 4. UV-vis diffuse reflectance absorption spectra of $\text{BiOCl}_x\text{I}_{1-x}$ prepared in EG and water. Insets show the digital camera images for the corresponding samples.

natures of 3D-BiOCl (EG) and 3D-BiOCl_{0.6}I_{0.4} were evidenced by the corresponding electron diffraction patterns. The energy-dispersive X-ray spectroscopy (EDX) data confirmed the elemental compositions for the two catalysts. The HRTEM image of 3D-BiOCl shows the lattice fringes with spacings of 0.277 nm and 0.350 nm corresponding to {1 1 0} and {0 1 1} facets, respectively.

3.3. UV-vis absorption and band gaps

The UV-vis reflectance absorption spectra for the $\text{BiOCl}_x\text{I}_{1-x}$ prepared in EG and water are displayed in Fig. 4. The Y-axis (absorbance) was converted from the diffuse reflectance value by the Kubelka-Munk method. The absorption edge (or the band gap) was determined by the intersection of the two extrapolated straight lines from the plots of $[\alpha h\nu]^{1/2}$ versus $h\nu$ (data not shown). The band gaps for BiOCl (EG and water) were measured to be 3.1–3.2 eV, which is consistent with the values reported in previous studies [12,18,19]. It is well known that the band gap depends on size, morphology, and crystallinity. Xiong et al. reported a band gap of 2.92 eV for square-like BiOCl nanoplates, and attributed the smaller band gap to a quantum confinement

effect [13]. For BiOCl prepared in ethanol (Supporting Info. Fig. S1), the UV-vis absorption was slightly enhanced in the visible region. Upon introduction of iodine, the band gap was significantly decreased. The band gaps of 3D flower-like (synthesized in EG) and 2D plate-like (synthesized in water) $\text{BiOCl}_{0.4}\text{I}_{0.6}$ were measured to be 2.1 and 1.9 eV, respectively. Since the absorption in the visible region was increased upon loading iodine, the photocatalytic performance under visible light is expected to be enhanced. Qin et al. performed visible light photocatalytic experiments using BiOX hierarchical microspheres for the removal of MO, which resulted in a performance order of $\text{BiOCl} < \text{BiOBr} \ll \text{BiOI}$. They attributed the higher activity of BiOI to more visible light absorption [7].

3.4. Raman spectra

Fig. 5 displays the Raman spectra of $\text{BiOCl}_x\text{I}_{1-x}$ ($0 \leq x < 1$) prepared in water and EG. The FT-IR spectra are shown in the Supporting Info., Fig. S3. The Raman spectra show three peaks as commonly found, and summarized in Table 1. The Raman peaks for the 3D flower-like $\text{BiOCl}_x\text{I}_{1-x}$ (EG) were broader than those of 2D $\text{BiOCl}_x\text{I}_{1-x}$ (EG) in accordance with the XRD results.

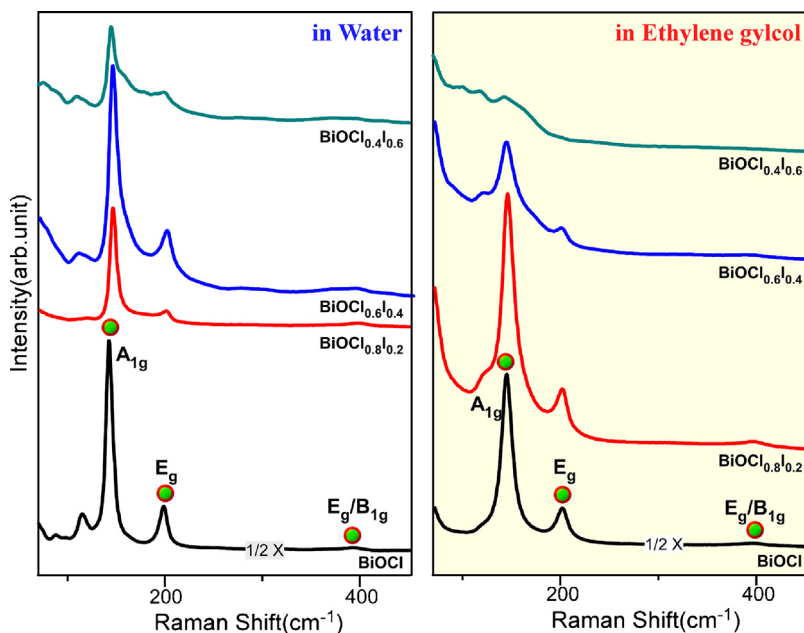


Fig. 5. Raman spectra of $\text{BiOCl}_x\text{I}_{1-x}$ prepared in water and EG.

Table 1

The observed Raman shifts (cm^{-1}) of $\text{BiOCl}_x\text{I}_{1-x}$ prepared in water and EG.

$\text{BiOCl}_x\text{I}_{1-x}$ samples	Water				EG			
	$x=1$	$x=0.8$	$x=0.6$	$x=0.4$	$x=1$	$x=0.8$	$x=0.6$	$x=0.4$
A_{1g} (cm^{-1})	144.5	145	144.5	145	143	144	143	142.5
E_g (cm^{-1})	200.5	199.5	200.5	198.5	200	200	199	
E_g/B_{1g} (cm^{-1})	394	398	393.5	387.5	394.5	393	392.5	393.5

The strongest peak at $\sim 144 \text{ cm}^{-1}$ was assigned to the overlapping of A_{1g} mode (internal Bi–Cl stretching), while the peak at $\sim 200 \text{ cm}^{-1}$ was assigned to E_g mode (internal Bi–Cl stretching). The weakest peak at around 390 cm^{-1} was attributed to the E_g/B_{1g} modes of oxygen atoms [5,10,22]. For BiOCl with a tetragonal structure (P4/mmm), the vibration modes are described as $\Gamma = 2\text{A}_{1g} + \text{B}_{1g} + 3\text{E}_g + 2\text{E}_{u} + 2\text{A}_{2u}$, where A_{1g} , B_{1g} , and 3E_g are Raman active, and others are IR active [2,12,22]. With increasing the iodine composition, the Raman bands become broader and significantly weaker, reflecting poor crystallinity resulting from a mixed composition, which is stronger for the samples prepared in EG.

3.5. Adsorption and photocatalytic activity of methyl orange

We tested the adsorption performance of the $\text{BiOCl}_x\text{I}_{1-x}$ (synthesized in EG and water) catalysts (Fig. 6). The corresponding UV-vis absorption spectra are shown in the bottom of Fig. 6 for the selected samples {i.e. BiOCl (synthesized in water) and $\text{BiOCl}_{0.6}\text{I}_{0.4}$ (synthesized in EG)}. The absorption peak at 460 nm is associated with the azo bond ($-\text{N}=\text{N}-$) and used to examine

the adsorption/photocatalysis performance. For the 2D plate-like BiOCl (water), the UV-vis absorption intensity was decreased by only about 5% after 160 min of adsorption under dark condition. With increasing iodine in 2D plate-like $\text{BiOCl}_x\text{I}_{1-x}$ (water) catalyst, the UV-vis absorption intensity decreased by 10–20%. For the 3D flower-like BiOCl (EG), the adsorption performance was greatly enhanced, and the UV-vis absorption intensity was decreased by about 30%. Upon introduction of iodine, the adsorption performance increased drastically, and the dye was adsorbed by more than 90% within 5–30 min. For the $\text{BiOCl}_{0.6}\text{I}_{0.4}$ catalyst, the MO dye was almost completely removed in 30 min by adsorption as shown in Fig. 6. The observed adsorption ability was found to be in the order of 2D BiOCl (water) < 2D $\text{BiOCl}_{0.8}\text{I}_{0.2}$ (water) ~ 2D $\text{BiOCl}_{0.4}\text{I}_{0.6}$ (water) < 2D $\text{BiOCl}_{0.6}\text{I}_{0.4}$ (water) < 3D BiOCl (EG) ≪ 3D $\text{BiOCl}_{0.8}\text{I}_{0.2}$ (EG) < 3D $\text{BiOCl}_{0.6}\text{I}_{0.4}$ (EG) ≈ 3D $\text{BiOCl}_{0.4}\text{I}_{0.6}$ (EG). After the adsorption test, we measured the reflectance UV-vis absorption spectra (Supporting Info. Fig. S4) of the used catalyst. Fig. S4 shows the UV-vis absorption peak for MO indicating that MO had been adsorbed onto the catalyst. The UV-vis absorption intensity of the adsorbed MO was in the order of 2D BiOCl (water) < 3D BiOCl (EG) ≪ 3D $\text{BiOCl}_{0.4}\text{I}_{0.6}$ (EG) for the used catalysts, which is consistent with the adsorption performance discussed above. We then washed the catalysts with deionized water to remove the adsorbed MO. The 2D plate-like catalysts turn to its original white color upon washing a couple of times. However, 3D flower-like catalysts required more than ten washes to recover the white color. The catalyst surface was also found to be clearly changed upon dye adsorption (Supporting Info. Fig. S5).

3.6. BET surface areas and adsorption

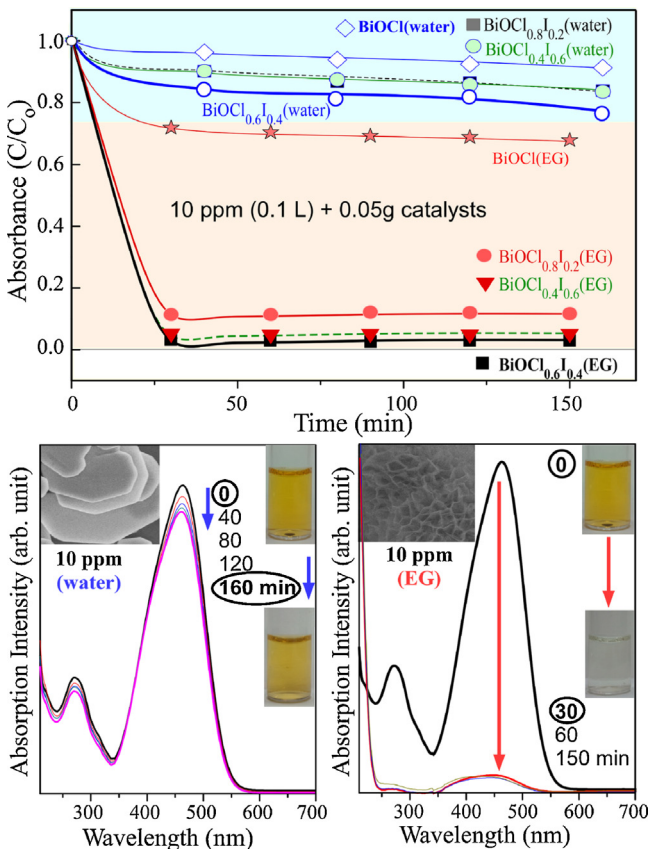
We selected three different samples (BiOCl prepared in EG and water, and $\text{BiOCl}_{0.6}\text{I}_{0.4}$ in EG) to measure the Brunauer–Emmett–Teller (BET) surface area as summarized in Table 2. The measured surface area was $5.5 \text{ m}^2/\text{g}$ for the 2D plate-like BiOCl (water). Xiong et al. reported a BET surface area of $8.1 \text{ m}^2/\text{g}$ for square-like BiOCl [13]. For 3D flower-like BiOCl (EG), the surface area increased (by $1.47\times$) to $16.8 \text{ m}^2/\text{g}$. As shown in the SEM images (Fig. 1), the flower-like BiOCl (EG) showed spongy structures with pores and consequently exhibited a larger surface area than the 2D plate-like BiOCl (water), as expected. The surface area was further increased by $2.77\times$ to $46.6 \text{ m}^2/\text{g}$ upon introducing iodine for $\text{BiOCl}_{0.6}\text{I}_{0.4}$ (EG). For $\text{BiOCl}_x\text{I}_{1-x}$ ($0 \leq x \leq 1$) reported by Dong et al., the specific BET surface areas were reported to be in the range of $5.71 (\text{BiOI})$ – $17.40 (\text{BiOCl}_{0.75}\text{I}_{0.25})$ [10]. Peng et al. prepared BiOCl microspheres, microflowers, microdisks, and microplates by hydrothermal methods, and reported BET surface areas of 61.8 , 53.5 , 13.5 , and $4.1 \text{ m}^2/\text{g}$, respectively [16]. The measured BET surface areas were in good correlation with the adsorption performances of MO as shown in Fig. 6.

Table 2

Summarized BET surface areas for the three selected samples.

Catalysts	2D- BiOCl	3D- BiOCl	3D- $\text{BiOCl}_{0.6}\text{I}_{0.4}$
Surface area (m^2/g)	5.5	16.8	46.6

Fig. 6. Top: adsorption ability of 50 mg $\text{BiOCl}_x\text{I}_{1-x}$ catalyst for MO (10 mg/mL, 100 mL) under dark. Bottom: UV-vis spectra of dye solution collected after the specified time are displayed for the 2D plate-like BiOCl (water) and 3D flower-like $\text{BiOCl}_{0.6}\text{I}_{0.4}$ (EG).



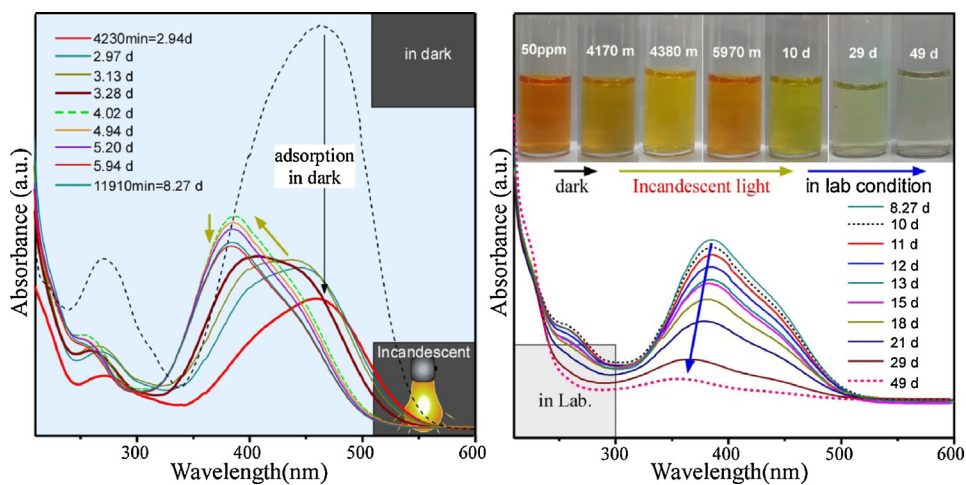


Fig. 7. UV-vis absorption plots showing the photodegradation of MO (50 mg/mL in 100 mL solution in a 250 mL flask) in the presence of 50 mg $\text{BiOCl}_{0.6}\text{I}_{0.4}$ in incandescent light and bright lab conditions. Top insets of the right plot show the digital camera photographs displaying change in dye color at different conditions. (For interpretation of the references to color in this figure legend, the reader is referred to the web version of the article.)

Since the MO dye was adsorbed rapidly on $\text{BiOCl}_{0.6}\text{I}_{0.4}$ (50 mg) catalyst in 10 mg/L dye solution, we increased the dye concentration to 50 mg/L and tested the adsorption/photocatalytic degradation performance as a function of time as shown in Fig. 7 (left). Upon complete adsorption of a dye in 2.94 days, we irradiated the dye solution mixed with catalyst under incandescent light. Interestingly, upon irradiation, the UV-vis absorption band was initially increased, after which it shifted to a shorter wavelength. Once the band was positioned at ~ 380 nm, the band gradually decreased with irradiation. However, the band was not decreased significantly after 5.94 days (Supporting Info. Fig. S6). Since we observed no significant change in UV-vis absorption intensity, we placed the sample near the window of our laboratory (normal daylight condition: fluorescent light + sunlight through the lab window). After 8.27 days, the UV absorption band due to dye was found to be gradually decreased with the time, and the MO was almost degraded in 49 normal days (no light during the morning, evening and night hours). This suggests that the photodegradation in daylight was more efficient than incandescent light. Since we used mild daylight, the complete degradation time was much longer than that reported in previous studies [13,19,21,23,28]. In addition, since we used a highly concentrated dye solution, the chance of light absorption directly by the catalyst was low; therefore, the photocatalytic activity will also be low. Without the catalyst under the same light conditions, no critical change in dye degradation was observed as studied by the UV-vis absorption spectroscopy.

3.7. Adsorption and photocatalytic activity of Rhodamine B

We further tested the adsorption/photodegradation of RhB. The left and right plots of Fig. 8 show the UV-vis absorption spectra of RhB with $\text{BiOCl}_{0.6}\text{I}_{0.4}$ under dark and bright conditions kept for different times, respectively. Since RhB shows the major UV-vis absorption band at 550 nm, the incandescent light can easily be absorbed, but not much was directly absorbed by the $\text{BiOCl}_{0.6}\text{I}_{0.4}$ catalyst. Upon adsorption for 5 min in the dark, the absorption peak decreased by more than 15%, indicating that the catalyst shows quicker adsorption of MO than RhB. For >1 day of adsorption, the absorption band was decreased by about 35%. However, the band was not critically changed even though we subjected it to adsorption for 2 days. Upon irradiation with incandescent light for 3 h, the absorption intensity was drastically decreased by $>60\%$ (right, Fig. 8). In addition, the peak position was shifted from 550 nm to 525 nm. As the irradiation time increased to 6 h, the absorption peak became narrower, while the intensity increased and the position shifted to 500 nm. Further increasing the irradiation from 8 to 32 h resulted in the narrower and smaller absorption peak. Upon further irradiation, the band gradually diminished, but the change was not as drastic as observed in the very early stage of 5 min–5 h. After 20 days of irradiation, the RhB was found to be completely photodegraded (Supporting Info. Fig. S7). In case of RhB, the electron in its occupied energy level can be excited to the unoccupied energy level under incandescent light and after which the electron in the

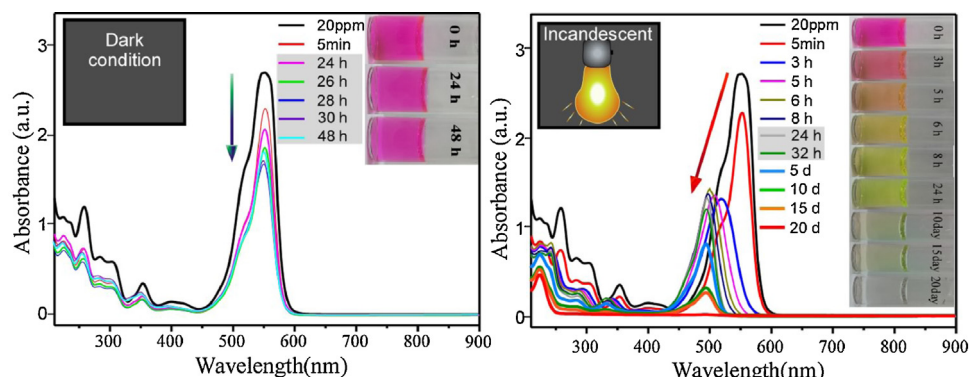


Fig. 8. Adsorption tests (left) of Rhodamine B (20 mg/L, 100 mL) in dark, and photodegradation test (right) in incandescent light and under bright conditions with 50 mg $\text{BiOCl}_{0.6}\text{I}_{0.4}$. Insets show the corresponding digital camera photographs displaying change in dye color with time. (For interpretation of the references to color in this figure legend, the reader is referred to the web version of the article.)

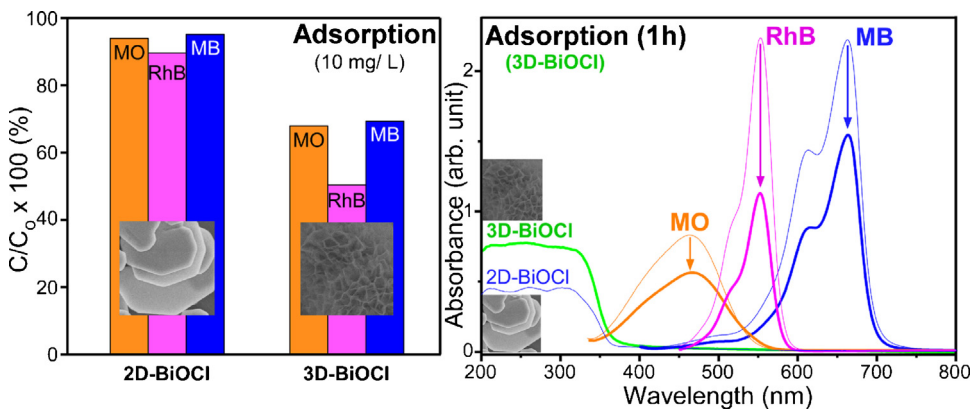


Fig. 9. Adsorption performances (left) of MO, RhB and MB after 1 h for 2D-BiOCl and 3D-BiOCl, and the corresponding UV-vis absorption spectra.

excited state could be transferred to the CB of the $\text{BiOCl}_{0.6}\text{I}_{0.4}$ catalyst. The RhB^+ then reacts with reactive radicals to be degraded [13], as discussed in detail below.

3.8. Photocatalytic activity of MO, RhB and MB under UV and visible lights

Since the photodegradation rate at a high concentration of dye was significantly low [29], we decreased the dye concentration, and further systematically performed the photodegradation experiments with MO, RhB and MB under irradiation of UV ($\lambda < 420 \text{ nm}$) and visible ($\lambda > 420 \text{ nm}$) lights. As discussed above, the adsorption performance of 3D-BiOCl was superior to that of 2D-BiOCl, as displayed in Fig. 9. RhB was found to be adsorbed more efficiently than

MO and MB, which is attributed to different electrostatic interactions of the dye [7].

Fig. 10 displays the photocatalytic degradation performances of MO, RhB and MB under UV and visible lights for 2D-BiOCl (water) and 3D-BiOCl (EG). As shown in the Figure, MB was poorly degraded under both UV and visible lights, compared with MO and RhB. MB was slightly more degraded under visible light irradiation with 3D-BiOCl. On the other hand, MO was more efficiently degraded under UV light than under visible light in presence of 3D-BiOCl. Interestingly, RhB with 3D-BiOCl was completely degraded in 2 h under visible light irradiation. However, the 2D-BiOCl showed a poor photocatalytic performance under visible light. Under visible light irradiation, the 3D and 2D-BiOCl showed a very similar RhB degradation performance. This result confirms that a dye sensitized mechanism is valid under visible light irradiation. In the

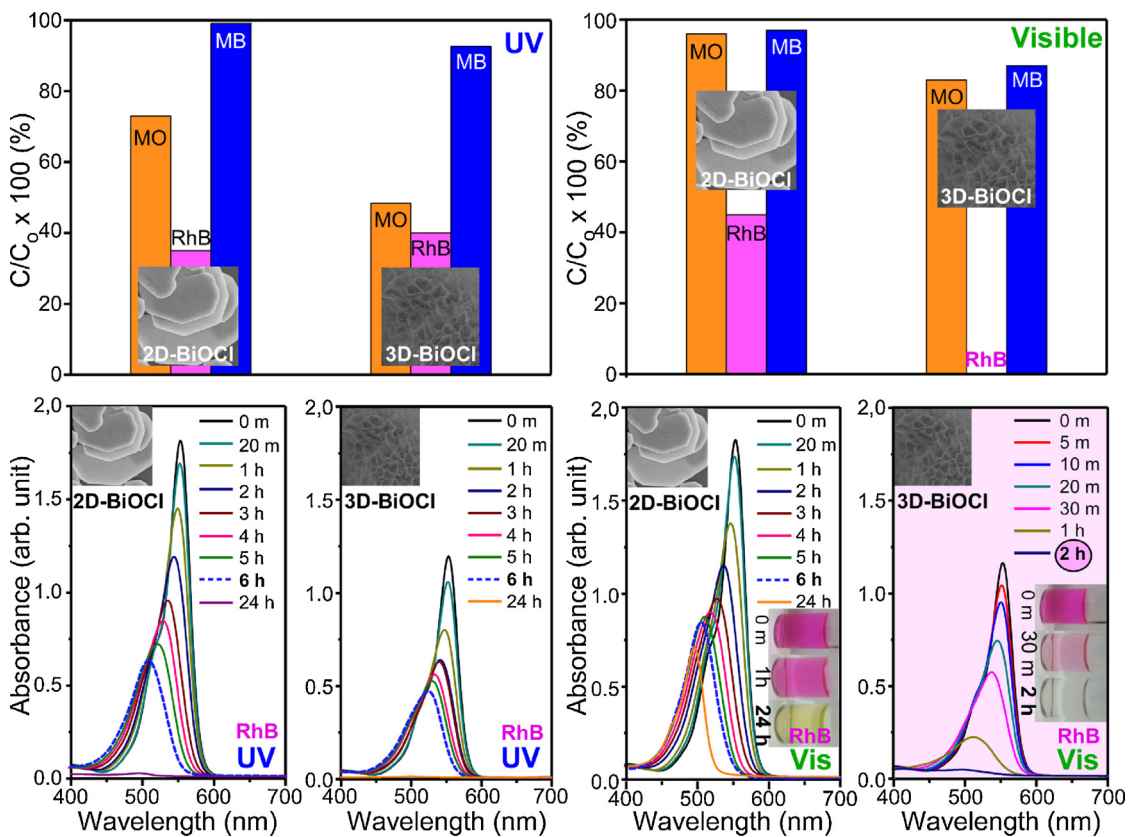


Fig. 10. Photocatalytic degradation of MO, RhB and MB under UV (top left) and visible (top right) light after 6 h with 2D-BiOCl (water) and 3D-BiOCl (EG), and the corresponding absorption spectra (bottom).

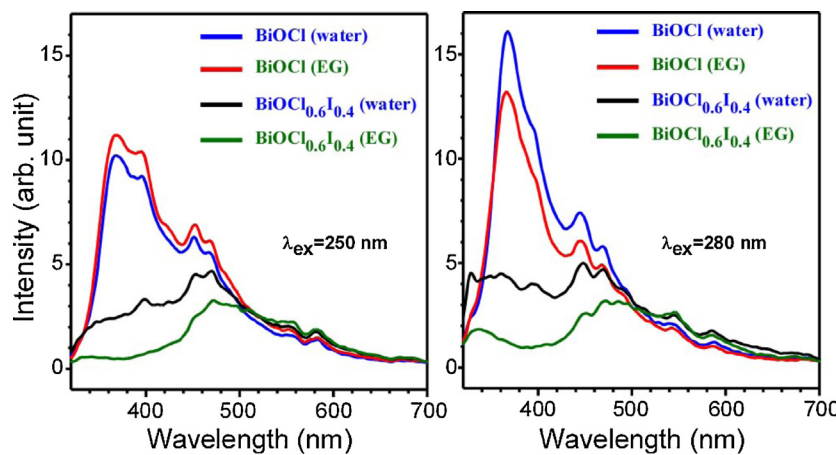


Fig. 11. Photoluminescence spectra of BiOCl and BiOCl_{0.6}I_{0.4} prepared in water and EG at excitation wavelengths of 250 (left) and 280 nm (right).

dye sensitized mechanism, exposed crystal facets and adsorption performance play important role in the photodegradation performance.

3.9. Photoluminescence spectra and electron–hole recombination

Fig. 11 displays the photoluminescence (PL) spectra of BiOCl and BiOCl_{0.6}I_{0.4} prepared in water and EG at two excitation wavelengths. The PL of a catalyst has been used to predict the photocatalytic efficiency. It is commonly believed that higher electron–hole recombination (or higher PL intensity) leads to poor charge separation efficiency, resulting in lower catalytic performance [15]. In the PL spectra, two broad regions were commonly observed at 370 nm and 460 nm [22]. For BiOCl (EG and water), the peak at 370 nm was dominant. At an excitation wavelength of 250 nm, the major PL peak of 3D flower-like BiOCl (EG) was stronger than that of 2D plate-like BiOCl (water). At an excitation wavelength of 280 nm, the intensity ratio became reversed, with the PL peak at 370 nm for 2D plate-like BiOCl (water) becoming stronger. Jiang et al. synthesized BiOCl nanosheets with dominant exposed {0 0 1} facets and found that they exhibited higher photocatalytic activity under UV irradiation, while BiOCl with dominant {0 1 0} facets showed superior activity under visible light irradiation [15]. These findings indicate that the relative PL intensity (or the relative catalytic activity) is different for materials with different exposed facets under irradiation of different photon energies. For the BiOCl_{0.6}I_{0.4} catalysts, the PL intensity was significantly

decreased when compared with that of BiOCl. This reflects a higher catalytic activity for the BiOCl_{0.6}I_{0.4} catalyst, which is consistent with the present experimental results discussed above. The PL maxima were positioned at a longer wavelength of around 460 nm. This is due to a shift in band edge to a longer wavelength with increasing iodine composition, as shown in Fig. 4.

3.10. Major active species and photocatalytic mechanism

During the photocatalytic dye degradation process, many active intermediate species such as hydroxyl radicals ($\bullet\text{OH}$), superoxide radicals ($\bullet\text{O}_2^-$), electrons (e^-) and holes (h^+) are created. To detect these species and clearly understand photodegradation mechanism of the dye, DMPO (5,5-dimethyl-1-pyrroline N-oxide) electron paramagnetic resonance (EPR) spin trapping techniques could be considered, where active intermediates are revealed by tracking active spin species such as DMPO- $\bullet\text{OH}$ and DMPO- $\bullet\text{O}_2^-$ [27,30,31]. Fang et al. employed a ESR spin trapping technique and ¹⁸O isotope labeling method to analyze the photoreaction of organic compounds for BiOBr catalyst [31]. Xu et al. have efficiently employed LC-MS and LC-SIR (selected ion recording)-MS to detect reaction products and intermediates, and proposed reaction pathways for the photocatalytic degradations of tetrabromobisphenol [32] and carbamazepine [33]. Here, we employ alternative chemical methods to understand the photodegradation mechanism as follows. By adding scavengers of active species during the photodegradation experiments [25–27], the role of the active species in

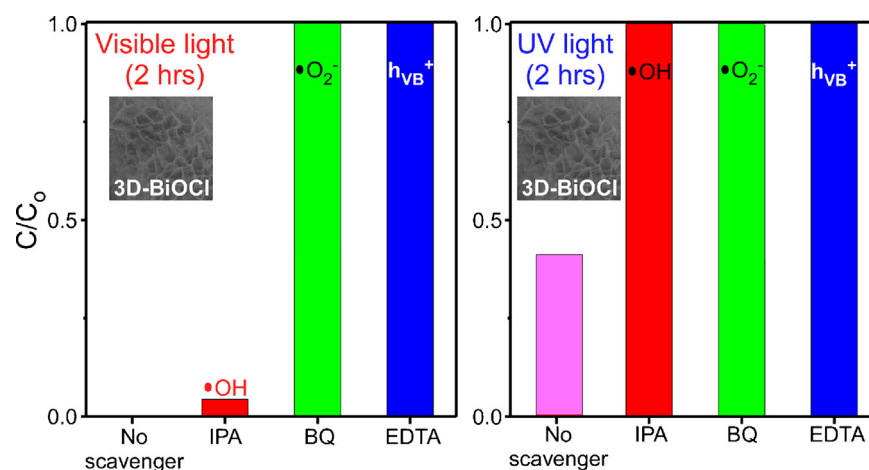


Fig. 12. Photocatalytic degradation of RhB with 3D-BiOCl in the absence and presence of scavengers (IPA, BQ, EDTA) under UV (right) and visible (left) lights for 2 h.

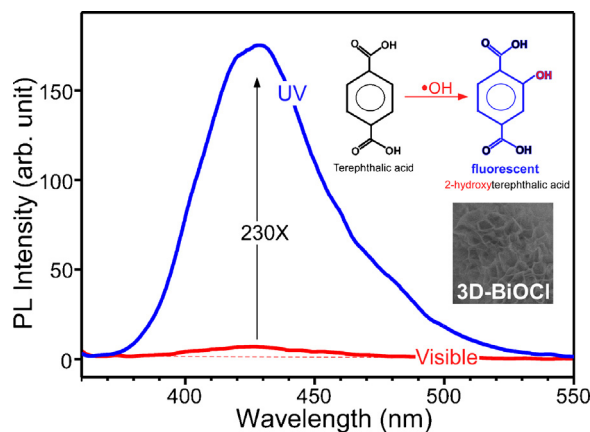


Fig. 13. Photoluminescence spectra of terephthalic acid solution with 3D-BiOCl catalyst after irradiations of UV and visible lights for 3 h.

photocatalytic mechanism can be obtained. Therefore, we used isopropyl alcohol (IPA), benzoquinone (BQ) and EDTA as scavengers for $\cdot\text{OH}$, $\cdot\text{O}_2^-$ and h^+ , respectively.

Fig. 12 displays photodegradation performance of 3D-BiOCl for RhB (10 mg/L) upon addition of various scavengers, and compared with the case without scavenger under irradiation of visible (>420 nm) light for 2 h. Upon addition of EDTA (h^+ scavenger), the degradation of RhB was almost totally suppressed. BQ ($\cdot\text{O}_2^-$ scavenger) also suppressed the dye degradation. However, IPA ($\cdot\text{OH}$ scavenger) showed no significant influence under visible light irradiation. Interestingly, under UV light, IPA significantly suppressed the dye degradation. This indicates that $\cdot\text{OH}$ is a major active species under UV light, but not under visible light.

Photoluminescence technique was further employed to tract $\cdot\text{OH}$ radicals photochemically formed in liquids using terephthalic acid (TA) [26,33]. TA reacts with $\cdot\text{OH}$ to produce 2-hydroxyterephthalic acid, which emits a broad luminescence at around 425 nm. Since $\cdot\text{OH}$ radical is produced during the photoirradiation the luminescence signal will be increased upon photoirradiation. Fig. 13 shows the photoluminescence results upon irradiation of UV and visible lights for 3 hrs. The photoluminescence was significantly increased under UV irradiation, while the intensity under visible light was very weak. This indicates that $\cdot\text{OH}$ plays an important role under UV irradiation. This is in good consistent with the result shown in Fig. 12. On the basis of these results, we could conclude that the active species play roles in the order of $\cdot\text{OH} \approx \cdot\text{O}_2^- \approx \text{h}^+$ and $\cdot\text{OH} \ll \cdot\text{O}_2^- \approx \text{h}^+$ for the photodegradation of a dye under UV and visible light irradiations, respectively.

On the basis of the photodegradation results with a scavenger, and the photoluminescence results, we propose the following photodegradation mechanism [26,34].

Under visible light irradiation ($\lambda > 420$ nm):

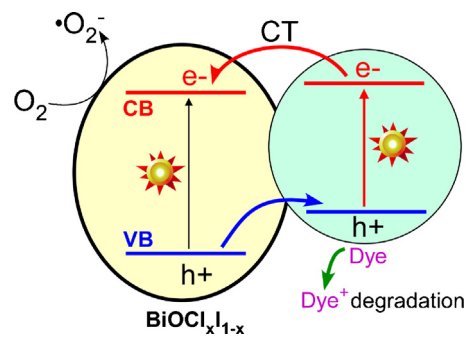
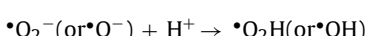
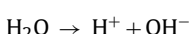
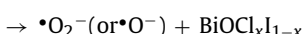
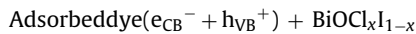
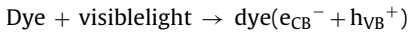
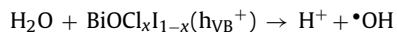
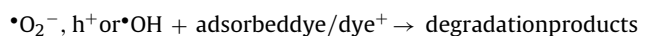
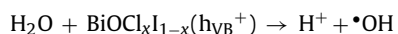
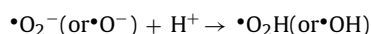
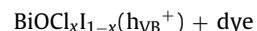
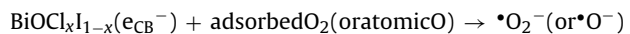
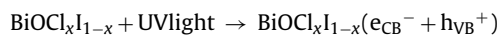


Fig. 14. Photocatalytic degradation mechanism of a dye on the $\text{BiOCl}_{x}\text{I}_{1-x}$ catalyst.



Under visible light irradiation, a dye sensitized mechanism has plausibly been proposed [25], depicted in Fig. 14. Upon irradiation of visible light, a dye absorbs the light to create an electron and a hole in the conduction and valence bands (CB and VB) of the dye. The electron in the CB then transfers to the CB of the catalyst. For a free dye molecule, the electron and the hole are quickly recombined before being used as an active species. Consequently, no photocatalytic activity was observed without a catalyst. Since the electron transfer rate determines the photodegradation performance [30] the adsorption of the dye and the exposed facets become the important factors to determine the charge transfer rate. The adsorbed molecular (or surface atomic) oxygen (an electron acceptor) on the catalyst captures the electron in the CB to form active $\cdot\text{O}_2^-$ (or O^-), which acts as an oxidant. In that case, dissolved oxygen in the dye solution will be an important factor [35]. The oxidant radical reacts with adsorbed dye to degrade it, or further proceed to form active $\cdot\text{OH}$ radicals. The VB holes react with adsorbed OH^- species to form $\cdot\text{OH}$ radicals. However, the formation channel to $\cdot\text{OH}$ is minor under visible light. The $\text{BiOCl}_{x}\text{I}_{1-x}$ also directly absorbs visible light to create an electron and a hole in CB and VB of the catalyst, and to further create active species.

Under UV light irradiation ($\lambda < 420$ nm):



Under UV light, the catalyst directly absorbs the light to create an electron and a hole in the CB and VB, respectively. Similarly, the electron in the CB and surface oxygen forms $\cdot\text{O}_2^-$ radicals. The hole in the VB migrates to the catalyst surface, and reacts with adsorbed

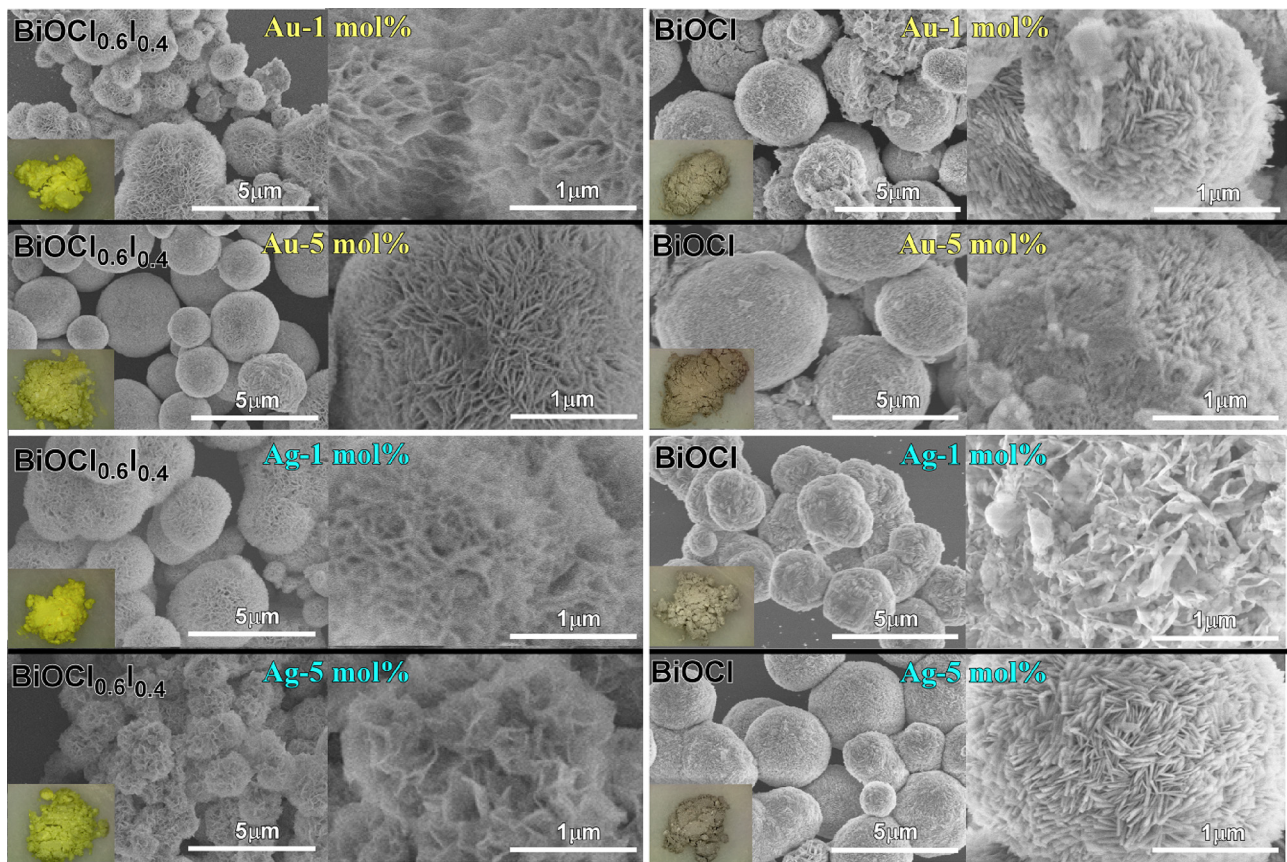


Fig. 15. SEM images of Ag and Au-doped (1 and 5 mol%) $\text{BiOCl}_{0.6}\text{I}_{0.4}$ (left two columns) and BiOCl (right two columns) prepared in EG. The doping concentrations were 1 and 5 mol%.

OH^- species to form $\cdot\text{OH}$ radical. The $\cdot\text{OH}$ species were found to be important under UV light irradiation, as discussed in Figs. 12 and 13. Consequently, three O_2^- , h^+ and $\cdot\text{OH}$ species play important roles in the dye degradation.

3.11. Morphology of Au and Ag-doped catalysts

We further examined the metal doping effect on the adsorption/photocatalytic activity of BiOCl . Fig. 15 shows the SEM images of Au and Ag-doped (1 and 5 mol%) BiOCl (EG) and $\text{BiOCl}_{0.6}\text{I}_{0.4}$ (EG) catalysts. For the Au and Ag-doped $\text{BiOCl}_{0.6}\text{I}_{0.4}$ (EG) catalysts, the morphology was slightly changed, and the sample color turned pale grayish-yellow when compared with un-doped catalysts. For the Au and Ag-doped BiOCl (EG), the color clearly turned gray.

3.12. Crystal structure of Au and Ag-doped catalysts

Although the change in morphology could not be clearly differentiated by the SEM image, the XRD patterns showed a clear change upon metal doping, as displayed in Fig. 16. The XRD patterns confirmed that AgI and AgCl formation occurs upon introducing Ag into $\text{BiOCl}_{0.6}\text{I}_{0.4}$ and BiOCl , respectively. However, for Au-doped catalyst, Au was present as metallic state. The (1 1 1), (2 0 0) and (2 2 0) planes of metallic Au were assigned to the corresponding diffraction peaks. The (1 0 0), (0 0 2) and (1 1 0) planes of AgI could be assigned based on the corresponding peaks. The other XRD features correspond to those of BiOCl , as shown in Fig. 2.

3.13. UV-vis absorption of Au and Ag-doped catalysts

Fig. 17 shows the UV-vis absorption spectra of Ag and Au-doped (1 and 5 mol%) $\text{BiOCl}_{0.6}\text{I}_{0.4}$ and BiOCl catalyst prepared in EG. The

absorption edge was found to be shifted to a longer wavelength for the Ag and Au-doped $\text{BiOCl}_{0.6}\text{I}_{0.4}$ catalyst, indicating an increase in absorption in the visible region. However, no critical change in band edge was observed for the doped BiOCl samples, indicating a negligible doping effect on the optical property/bandgap.

3.14. Adsorption, BET, and photodegradation of MO with Au and Ag-doped catalysts

We tested the MO adsorption performances with the Ag and Au-doped $\text{BiOCl}_{0.6}\text{I}_{0.4}$ (EG) catalyst under dark conditions (Fig. 18). The MO adsorption performance was drastically degraded upon just 1 mol% doping. For undoped $\text{BiOCl}_{0.6}\text{I}_{0.4}$ (EG) catalyst, the MO dye (10 mg/L) was almost completely adsorbed and removed within 30 min, as shown in Fig. 6. The UV-vis absorption intensity was only decreased by 40% in 24 h, even for 1 mol% Ag-doped $\text{BiOCl}_{0.6}\text{I}_{0.4}$ (EG) catalyst. The 5 mol% Au and Ag-doped samples showed even poorer adsorption performance than the 1 mol% doped samples. The order of adsorption performance was 5 mol% Au \approx 5 mol% Ag $<$ 1 mol% Au $<$ 1 mol% Ag, which could be due to the reduction in surface charges [7] of the catalyst by metal doping. This leads to weaker electrostatic interactions between the charged ions of the dye and the catalyst resulting poor adsorption performance.

We selected 5 mol% Au and Ag-doped samples to measure the BET surface area as summarized in Table 3. The BET surface areas were found to be 18.8 (Au- $\text{BiOCl}_{0.6}\text{I}_{0.4}$), 49.1 (Ag- $\text{BiOCl}_{0.6}\text{I}_{0.4}$), 16.3 (Au- BiOCl), and 19.3 m^2/g (Ag- BiOCl) with 5 mol% Au or Ag. When compared with the undoped samples, no significant change in surface area was observed, except for the 5 mol% Au- $\text{BiOCl}_{0.6}\text{I}_{0.4}$, which showed a 2.47 decrease in surface area compared with that (46.6 m^2/g) of undoped 3D- $\text{BiOCl}_{0.6}\text{I}_{0.4}$. Actually, the BET surface areas of doped and undoped catalysts showed no good correlation

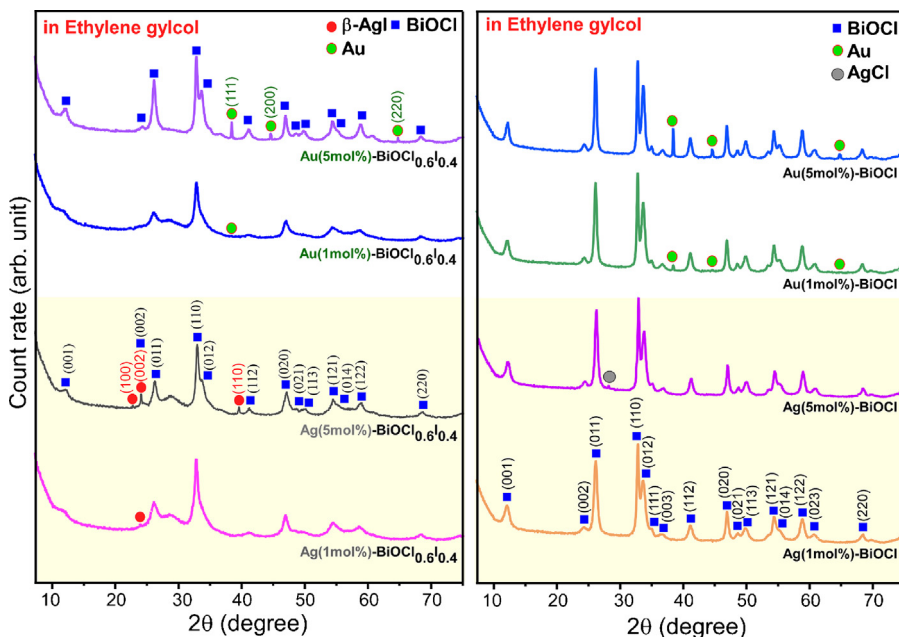


Fig. 16. Power X-ray diffraction patterns of Ag and Au-doped BiOCl_{0.6}I_{0.4} (left column) and BiOCl (right column) prepared in EG. The doping concentrations were 1 and 5 mol%.

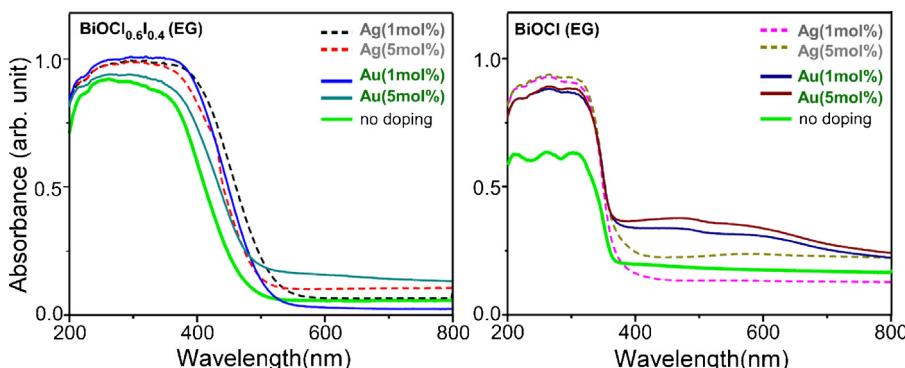


Fig. 17. UV-vis absorption spectra of Ag and Au-doped BiOCl_{0.6}I_{0.4} (left) and BiOCl (right) prepared in EG. The doping concentrations were 1 and 5 mol%.

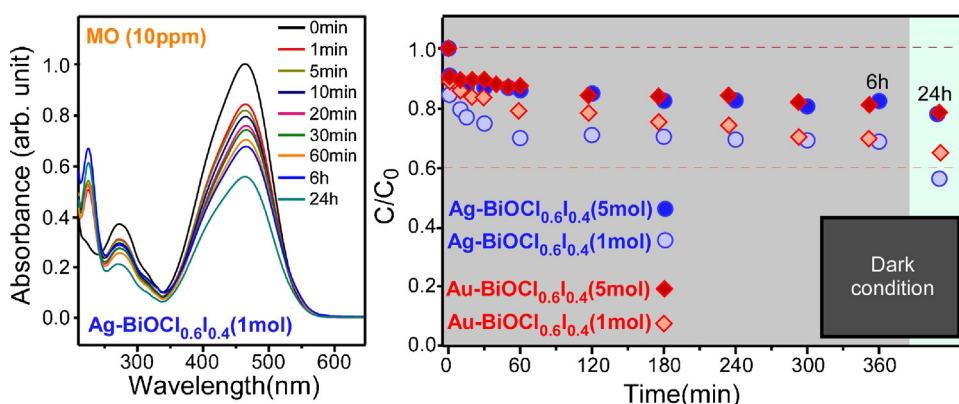


Fig. 18. Adsorption ability of 50 mg Ag and Au-doped BiOCl_{0.6}I_{0.4} (EG) catalyst for MO (10 mg/L, 100 mL) under dark conditions. UV-vis spectra with time are displayed for the selected samples of 1 mol% Ag-doped BiOCl_{0.6}I_{0.4} (EG).

Table 3

Summarized BET surface areas of Au and Ag-doped (5 mol%) BiOCl (EG) and BiOCl_{0.6}I_{0.4} (EG) catalysts, compared with 3D-BiOCl (EG).

Catalysts	Au-BiOCl	Ag-BiOCl	BiOCl	Au-BiOCl _{0.6} I _{0.4}	Ag-BiOCl _{0.6} I _{0.4}
Surface area (m ² /g)	16.3	19.3	16.8	18.8	49.1

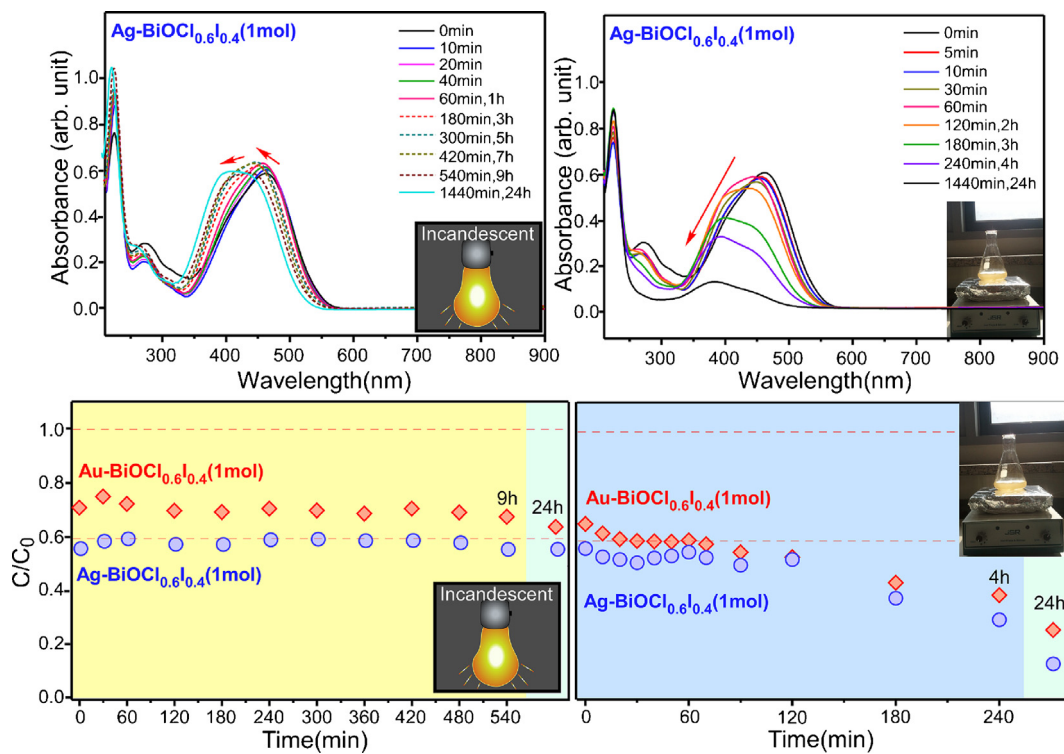


Fig. 19. Photodegradation of MO (10 mg/L, 100 mL) for 50 mg 1 mol% Ag and Au-doped BiOCl_{0.6}I_{0.4} (EG) catalyst in incandescent and sunlight through the lab window (see right inset photo). UV-vis spectra with time are displayed for the selected 1 mol% Ag-doped BiOCl_{0.6}I_{0.4} (EG).

with the adsorption performances. This indicates that the surface charge plays an important role in the adsorption of a dye. Since the charge transfer process is very important for the dye-sensitized mechanism (Fig. 14), intuitively good adsorption between the dye and the catalyst is important for the efficient photodegradation. For this reason, the poor dye adsorption with the metal-doped catalyst would lead to poor photocatalytic performance.

After adsorption of the MO dye for 24 h, we irradiated the Ag and Au doped BiOCl_{0.6}I_{0.4} (EG) catalyst by incandescent light or sunlight for 24 h. Fig. 19 (left) shows the UV-vis absorption spectra of MO dye after being degraded for a specified time in the presence of catalyst and incandescent light. Under incandescent light, the MO absorption peak was gradually shifted to a shorter wavelength with no critical change in intensity. Conversely, under daylight coming through the laboratory window, the MO absorption intensity decreased significantly, which was accompanied by a shift in peak position with time (Fig. 19, right).

To examine the role of active species during the photodegradation of RhB under visible light in presence of metal-doped BiOCl, the scavenger probe method was employed, as displayed in Fig. 20. As discussed above, the adsorption performances of Ag and Au-BiOCl were degraded. After adsorption for 1 h (Fig. 20, left), the RhB concentration with 3D-BiOCl was more decreased than that with 3D-Ag-BiOCl. Upon visible light irradiation, the RhB with 3D-BiOCl was completely degraded in 2 h while that with 3D-Ag-BiOCl was still remained in the solution. This result confirmed that the photodegradation performance was decreased after metal doping, in good agreement with a literature [36]. For the scavenger tests, the RhB solution containing BQ or EDTA was not degraded at all while the solution containing IPA was degraded the same amount as the solution without a scavenger. For a dye sensitized mechanism of the metal doped BiOCl, it could be concluded that $\bullet\text{O}_2^-$ and h^+ are the major active species under visible light irradiation.

3.15. Photoluminescence of Au and Ag-doped catalysts

Fig. 21 displays the photoluminescence of Ag and Au-doped BiOCl and BiOCl_{0.6}I_{0.4} prepared in EG. For the BiOCl_{0.6}I_{0.4} (EG) catalyst, the PL intensity was increased by 2–3 times upon Ag and Au doping. For the BiOCl (EG) catalyst, the PL intensity was increased upon metal doping. The peak position for the broad PL showed no critical change upon doping. However, a new sharp peak was appeared at around 330 nm at an excitation wavelength of 280 nm. We tentatively attributed this to a newly created site upon metal doping. The site acts as a charge recombination center to increase in photoluminescence from the doped samples. Based on the PL

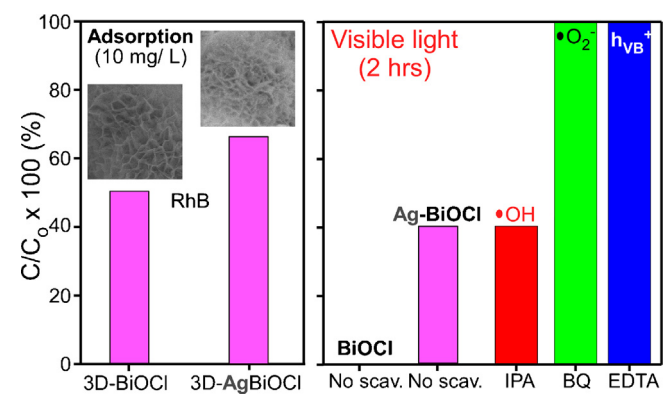


Fig. 20. Adsorption performances (left) of RhB with 3D-BiOCl and 3D-Ag (1 mol%)-BiOCl. Photocatalytic degradation (right) of RhB with 3D-Ag (1 mol%)-BiOCl in the absence and presence of scavengers (IPA, BQ and EDTA) under UV and visible lights, compared with undoped 3D-BiOCl.

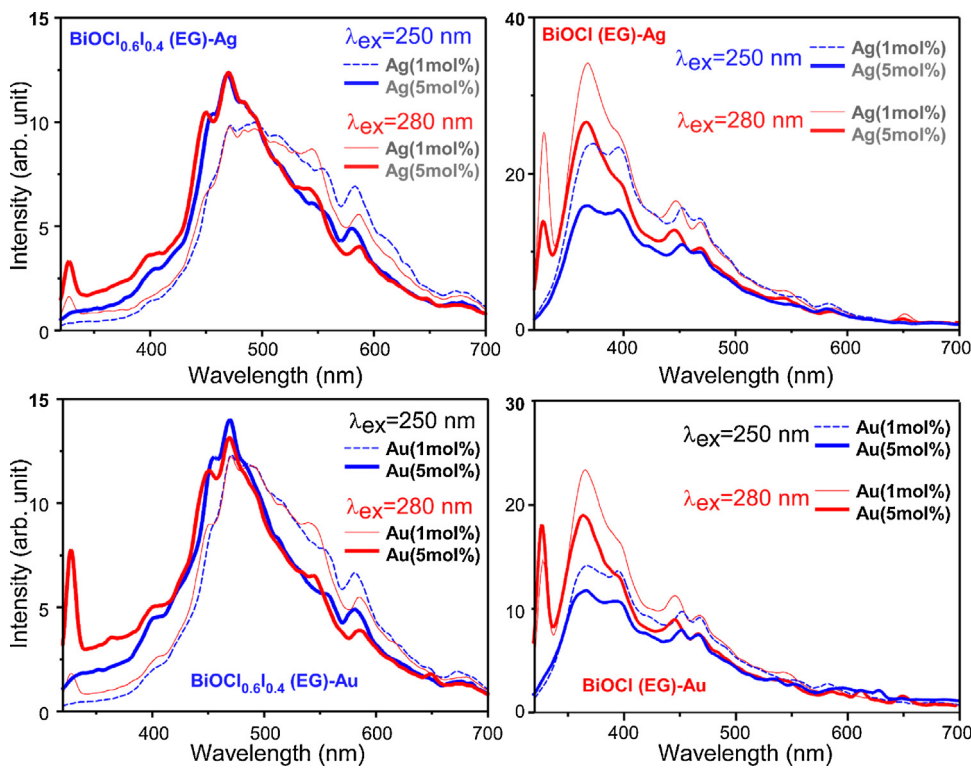


Fig. 21. Photoluminescence spectra of 1 and 5 mol% Ag (top) and Au-doped (bottom) $\text{BiOCl}_{0.6}\text{I}_{0.4}$ (left column) and BiOCl (right column) prepared in EG at excitation wavelengths of 250 and 280 nm.

results, the photocatalytic efficiency is likely to decrease for the metal doped catalysts.

4. Summary

We synthesized BiOCl and $\text{BiOCl}_x\text{I}_{1-x}$ catalysts using two different solvents, EG and water, and then examined their properties by SEM, XRD, UV-vis absorption, Raman, FT-IR, and PL spectroscopy. Their adsorption and photocatalytic performance were tested for MO and RhB dyes. The SEM images showed 3D flower-like and 2D plate-like structures obtained using EG and water solvents, respectively. We found that the adsorption and photocatalytic degradation performance of the 3D flower-like BiOCl is superior to 2D plate-like BiOCl structures. The adsorption and photocatalytic activity were further improved with iodine-containing $\text{BiOCl}_x\text{I}_{1-x}$ catalysts of similar morphology to the samples without iodine. The BET surface area was found to be in the order of 2D plate-like BiOCl ($5.5 \text{ m}^2/\text{g}$) < 3D BiOCl ($16.8 \text{ m}^2/\text{g}$) < $\text{BiOCl}_{0.6}\text{I}_{0.4}$ ($46.6 \text{ m}^2/\text{g}$). The Ag and Au-doped BiOCl and $\text{BiOCl}_x\text{I}_{1-x}$ catalysts were also synthesized and examined in detail. The PL intensity of $\text{BiOCl}_x\text{I}_{1-x}$ catalysts was significantly increased upon Ag or Au-doping. The dye adsorption performance of $\text{BiOCl}_x\text{I}_{1-x}$ catalysts was dramatically reduced upon loading with small amounts of Ag or Au-loading, which was tentatively attributed to a diminished surface charge of the catalyst. The photocatalytic degradation performance of the metal doped catalyst was understood by a dye-sensitized mechanism in correlation with adsorption and newly created recombination center. In the dye-sensitized photocatalytic mechanism, $\bullet\text{O}_2^-$ and h^+ were found to be the major active species, and $\bullet\text{OH}$ showed a minor contribution, as confirmed by an indirect chemical probe method using active species scavengers, and photoluminescence. Under UV light irradiation, the three $\bullet\text{O}_2^-$, h^+ and $\bullet\text{OH}$ species were all active for the photodegradation of the dyes. The results of the present study provide insight into development of adsorbents and photocatalysts for water purification and clean environmental projects.

Acknowledgements

This work was financially supported by the India-Korea joint project; the National Research Foundation of Korea (NRF) grant funded by the Korean government (MEST) (No. 2012-0006296), and the Department of Science and Technology, New Delhi through the Indo-Korea/P-02 grant.

Appendix A. Supplementary data

Supplementary material related to this article can be found, in the online version, at <http://dx.doi.org/10.1016/j.apcatb.2013.10.008>.

References

- [1] X. Zhang, X. Liu, C. Fan, Y. Wang, Y. Wang, Z. Liang, *Applied Catalysis B* 132–133 (2013) 332–341.
- [2] L. Zhang, W. Wang, S. Sun, Y. Sun, E. Gao, J. Xu, *Applied Catalysis B* 132–133 (2013) 315–320.
- [3] K. Li, Y. Tang, Y. Xu, Y. Wang, Y. Huo, H. Li, J. Jia, *Applied Catalysis B* 140–141 (2013) 179–188.
- [4] S. Peng, L. Li, P. Zhu, Y. Wu, M. Srinivasan, S.G. Mhaisalkar, S. Ramakrishna, Q. Yan, *Chemistry: An Asian Journal* 8 (2013) 258–268.
- [5] S. Weng, B. Chen, L. Xie, Z. Zheng, P. Liu, *Journal of Material Chemistry A* 1 (2013) 3068–3075.
- [6] J. Xiong, G. Cheng, F. Qin, R. Wang, H. Sun, R. Chen, *Chemical Engineering Journal* 15 (2013) 228–236.
- [7] X. Qin, H. Cheng, W. Wang, B. Huang, X. Zhang, Y. Dai, *Materials Letters* 100 (2013) 285–288.
- [8] H. Cheng, B. Huang, X. Qin, X. Zhang, Y. Dai, *Chemical Communication* 48 (2012) 97–99.
- [9] L. Ye, K. Deng, F. Xu, L. Tian, T. Peng, L. Zan, *Physical Chemistry Chemical Physics* 14 (2012) 82–85.
- [10] F. Dong, Y. Sun, M. Fu, Z. Wu, S.C. Lee, *Journal of Hazardous Materials* 219–220 (2012) 26–34.
- [11] F. Gao, D. Zeng, Q. Huang, S. Tianb, C. Xie, *Physical Chemistry Chemical Physics* 14 (2012) 10572–10578.
- [12] K. Zhang, J. Liang, S. Wang, J. Liu, K. Ren, X. Zheng, H. Luo, Y. Peng, X. Zou, X. Bo, J. Li, X. Yu, *Crystal Growth and Design* 12 (2012) 793–803.
- [13] J. Xiong, G. Cheng, G. Li, F. Qin, R. Chen, *RSC Advances* 1 (2011) 1542–1553.

- [14] S. Wu, C. Wang, Y. Cui, W. Hao, T. Wang, P. Brault, *Materials Letters* 65 (2011) 1344–1347.
- [15] J. Jiang, K. Zhao, X. Xiao, L. Zhang, *Journal of American Chemical Society* 134 (2012) 4473–4476.
- [16] Y. Tian, C.F. Guo, Y. Guo, Q. Wang, Q. Liu, *Applied Surface Science* 258 (2012) 1949–1954.
- [17] T.B. Li, G. Chen, C. Zhou, Z.Y. Shen, R.C. Jin, J.X. Sun, *Dalton Transactions* 40 (2011) 6751–6758.
- [18] X. Chang, J. Huang, C. Cheng, Q. Sui, W. Sha, G. Ji, S. Deng, G. Yu, *Catalysis Communication* 11 (2010) 460–464.
- [19] L.P. Zhu, G.H. Liao, N.C. Bing, L.L. Wang, Y. Yang, H.Y. Xie, *CrystEngComm* 12 (2010) 3791–3796.
- [20] J. Ma, X. Liu, J. Lian, X. Duan, W. Zheng, *Crystal Growth and Design* 10 (2010) 2522–2527.
- [21] F. Chen, H. Liu, S. Bagwasi, X. Shen, J. Zhang, *Journal of Photochemistry and Photobiology A* 215 (2010) 76–80.
- [22] S. Cao, C. Guo, Y. Lv, Y. Guo, Q. Liu, *Nanotechnology* 20 (2009) 275702.
- [23] Y. Lei, G. Wang, S. Song, W. Fan, H. Zhang, *CrystEngComm* 11 (2009) 1857–1862.
- [24] S.Y. Chai, Y.J. Kim, M.H. Jung, A.K. Chakraborty, D.W. Jung, W.I. Lee, *Journal of Catalysis* 262 (2009) 144–149.
- [25] J. Cao, B. Xu, H. Lin, B. Luo, S. Chen, *Chemical Engineering Journal* 185 (2012) 91–99.
- [26] J. Cao, B. Xu, H. Lin, B. Luo, S. Chen, *Dalton Transactions* 41 (2012) 11482–11490.
- [27] M. Yin, Z. Li, J. Kou, Z. Zou, *Environmental Science and Technology* 43 (2009) 8361–8366.
- [28] K.L. Zhang, C.M. Liu, F.Q. Huang, C. Zheng, W.D. Wang, *Applied Catalysis B* 68 (2006) 125–129.
- [29] B. Subash, B. Krishnakumar, M. Swaminathan, M. Shanthi, *Langmuir* 29 (2013) 939–949.
- [30] Y. Chen, D. Li, X. Wang, L. Wu, X. Wang, X. Fu, *New Journal of Chemistry* 29 (2005) 1514–1519.
- [31] Y.-F. Fang, W.-H. Ma, Y.-P. Huang, G.-W. Cheng, *Chemistry: A European Journal* 19 (2013) 3224–3229.
- [32] J. Xu, W. Meng, Y. Zhang, L. Li, C. Guo, *Applied Catalysis B* 107 (2011) 355–362.
- [33] J. Xu, L. Li, C. Guo, Y. Zhang, W. Meng, *Applied Catalysis B* 130–131 (2013) 285–292.
- [34] Y. Li, J. Wang, H. Yao, L. Dang, Z. Li, *Journal of Molecular Catalysis A* 334 (2011) 116–122.
- [35] L. Ye, L. Tian, T. Peng, L. Zan, *Journal of Material Chemistry* 21 (2011) 12479–12484.
- [36] L. Lu, L. Kong, Z. Jiang, H.H.-C. Lai, T. Xiao, P.P. Edwards, *Catalysis Letters* 142 (2012) 771–778.